Thermoelastic properties of microcracked polycrystals. Part I : Adequacy of Fourier-based methods for cracked elastic bodies

Jean-Baptiste Gasnier, François Willot, Hervé Trumel, Dominique Jeulin, Jacques Besson

▶ To cite this version:

Jean-Baptiste Gasnier, François Willot, Hervé Trumel, Dominique Jeulin, Jacques Besson. Thermoelastic properties of microcracked polycrystals. Part I : Adequacy of Fourier-based methods for cracked elastic bodies. International Journal of Solids and Structures, 2018, 155, pp.248-256. 10.1016/j.ijsolstr.2018.07.024 . hal-01932739v2

HAL Id: hal-01932739
https://hal.science/hal-01932739v2

Submitted on 1 Feb 2019

HAL is a multi-disciplinary open access archive for the deposit and dissemination of scientific research documents, whether they are published or not. The documents may come from teaching and research institutions in France or abroad, or from public or private research centers.

L'archive ouverte pluridisciplinaire **HAL**, est destinée au dépôt et à la diffusion de documents scientifiques de niveau recherche, publiés ou non, émanant des établissements d'enseignement et de recherche français ou étrangers, des laboratoires publics ou privés.

Thermoelastic properties of microcracked polycrystals. Part I: Adequacy of Fourier-based methods for cracked elastic bodies

Jean-Baptiste Gasnier[a], François Willot,*[a,b] Hervé Trumel[b], Dominique Jeulin[a,b] Jacques Besson[c]

[a]Mines ParisTech, PSL Research University, Centre for Mathematical Morphology, 35 rue Saint-Honoré, F-77300 Fontainebleau, France. [b]CEA, DAM, Le Ripault, F-37260 Monts, France. [c]Mines ParisTech, PSL Research University, Centre for Materials, 63-65 Rue Henri Auguste Desbruères, F-91100 Corbeil-Essonnes, France. *Corresponding author (`francois.willot@ensmp.fr`).

Reference: *International Journal of Solids and Structures* 155, 2018, 248–256 (`https://doi.org/10.1016/j.ijsolstr.2018.07.024`). The text in the present document is the same as in the published article, page layout is different. v2: The bibliographical data for one reference (previously marked as submitted and published since then) has been updated.

Abstract This study is part of a work dedicated to predicting the overall thermoelastic properties of microcracked polycrystals. In the present part, the suitability of Fourier-based methods to estimate the mechanical response of a homogeneous body containing cracks is explored. The effect of the Green operator's discretization on the local elastic fields surrounding the crack's tip is investigated and compared with exact and finite elements solutions. The biases inherent to the Fourier method, namely the effects of grid discretization and crack orientation relative to the grid, are scrutinized. A way to quantify and overcome these biases is given, therefore providing a low resource demanding method to deal with thousands of microcracks embedded in a polycrystal, object of the companion paper.

Keywords: Cracked media; Homogenization; Elasticity; Fourier-based Methods.

1 Introduction

Quasi-brittle materials, such as concrete, rocks, ceramics and many jointed or sintered materials, are well known to undergo microcracking prior to failure. Many authors have endeavored to model this effect in the context of continuum damage mechanics modeling, either phenomenologically (see, for instance Cormery and Welemane, 2002; Bargellini et al., 2008; Cormery and Welemane, 2010; Challamel, 2010), or by various micromechanical methods (see, for example Budiansky, 1976; Horii and Nemat-Nasser, 1983; Andrieux et al., 1986; Krajcinovic, 1989; Kachanov, 1992; Pensée and Kondo, 2003; Dormieux and Kondo, 2009; Zhu et al., 2011; Monchiet et al., 2012; Levasseur et al., 2015). The vast majority of these approaches consider the damaged medium as a population of microcracks embedded in a (possibly anisotropic) homogeneous matrix.

If the attention is restricted, from now on, to initially isotropic (possibly jointed and sintered) polycrystals, this assumption can be considered as legitimate for weakly anisotropic grains. In many other situations, however, it is too strong (see for instance Ortiz, 1985; Pijaudier-Cabot and Bazant, 1987; Challamel, 2010), and the polycrystalline nature of the matrix must be accounted for. This can be done through self-consistent modeling (Huang and Hu, 1994; Willot et al., 2018), as well as finite elements (see in particular the recent work of Yan et al. (2016) for polycrystalline graphite). In the first case, local fields are not available, whereas heavy computational resources are needed in the second case.

The aim of the present work is to study this problem using the Fourier-based (FFT) full-field homogenization technique, providing access to full fields and much less demanding than finite elements in terms of computational resources. By nature, however, FFT is not adapted to accounting for zero-volume objects such as cracks, and computational biases must be expected. As this method has very seldom been used for dealing with cracks (see Li et al., 2012a,b; Cheng, 2017), is it essential to assess such biases quantitatively, and to derive the means of accounting for them, which is the purpose of the present paper. In the companion paper, the method will be applied to a jointed polycrystal with strong thermoelastic anisotropy.

The present article is organized as follows. Fourier methods are first described in Section 2. The problem of a 2D, doubly-periodic array of cracks under plane strain is addressed in Section 3. Comparisons with finite element computations are carried out in Section 4. The effect of grid discretization, crack shape and orientation relative to the grid is discussed in Section 5. In this latter part, 3D media containing periodic and randomly-distributed cracks are considered. We conclude in Section 6.

2 Spectral methods for computing the mechanical response of cracked media

Consider the following linear-elastic problem, defined on a parallelepipedic domain Ω:

$$\begin{aligned} \boldsymbol{\sigma}(\boldsymbol{x}) &= \mathbf{C}(\boldsymbol{x}) : \boldsymbol{\varepsilon}(\boldsymbol{x}), && \text{(1a)} \\ \varepsilon_{ij}(\boldsymbol{x}) &= (1/2)\left[\partial_i u_j(\boldsymbol{x}) + \partial_j u_i(\boldsymbol{x})\right], \qquad \partial_i \sigma_{ij}(\boldsymbol{x}) \equiv 0, && \text{(1b)} \\ \langle \boldsymbol{\varepsilon}(\boldsymbol{x}) \rangle &= \overline{\boldsymbol{\varepsilon}}, \qquad \boldsymbol{\varepsilon}\ \#, \qquad \boldsymbol{\sigma} \cdot \mathbf{n} - \#, && \text{(1c)} \end{aligned}$$

where $\boldsymbol{u}(\boldsymbol{x})$, $\boldsymbol{\sigma}(\boldsymbol{x})$, $\boldsymbol{\varepsilon}(\boldsymbol{x})$ and $\mathbf{C}(\boldsymbol{x})$ are respectively the displacement, stress, strain and stiffness tensor at point $\boldsymbol{x}$ ($\boldsymbol{x} \in \Omega$). Periodic boundary conditions are specified in (1c): $\overline{\boldsymbol{\varepsilon}}$ is the applied strain, symbols $\#$ and $-\#$ denote Ω-periodicity and anti-periodicity respectively, $\mathbf{n}$ is the outward-directed normal along the frontier of Ω, and $\langle \cdot \rangle$ denotes a spatial mean over the computational domain Ω. The strain and stress tensors are accordingly extended as admissible and divergence-free fields over the entire space $\mathbb{R}^3$. Plane strain conditions are obtained when the elastic tensor $\mathbf{C}(\boldsymbol{x})$ is invariant by translation along the direction normal to the plane and when the principal strain directions for the overall strain $\overline{\boldsymbol{\varepsilon}}$ lie in the plane.

Problem (1) is solved using Fourier methods based on the "accelerated scheme" (Eyre and Milton, 1999; Michel et al., 2001). We consider three different discretization schemes for the Green operator in the Fourier domain, which monitors the approximation space for the strain, displacement and stress fields: the "trigonometric" discretization, used notably by Moulinec and Suquet (1994) and Michel et al. (2001), denoted (FFT-MS), and two finite-differences discretization schemes, the "backward and forward" (Willot and Pellegrini, 2008), denoted (FFT-BF), and the "rotated" method (Willot, 2015), denoted (FFT-R). In method (FFT-MS), the strain and stress fields, and the periodic part of the displacement are trigonometric polynomials defined in the continuum, whereas in the other two schemes (FFT-BF) and (FFT-R), the fields are known along a set of discrete points only, corresponding to the voxel centers or corners. Convergence rates are sensitive to an isotropic "reference" stiffness tensor with shear modulus μ^0 and bulk modulus κ^0, which is chosen by the user.

In the following sections, cracks are modeled as very thin porous inclusions where the stiffness tensor is set to zero ($\mathbf{C}(\boldsymbol{x}) \equiv 0$), thereby assuming that all cracks are open under the applied load. The elastic response of the embedding matrix is defined by a positive definite stiffness tensor. Section 4 makes use of the displacement vector field $\boldsymbol{u}$, which is compared to finite element estimates. The latter is computed directly from the strain field in a manner consistent with the employed discretization. Component u_1 reads, in 2D (plane strain) and in 3D:

$$u_1(\boldsymbol{q}) = \frac{1}{|\boldsymbol{k}|^4} \times \left\{ \begin{array}{r} \left(|k_1|^2 + 2|k_2|^2\right) k_1^* \varepsilon_{11}(\boldsymbol{q}) + \left(k_2^*\right)^2 \left[2k_2 \varepsilon_{12}(\boldsymbol{q}) - k_1 \varepsilon_{22}(\boldsymbol{q})\right], \\ (d=2), \\ \left(2|\boldsymbol{k}|^2 - |k_1|^2\right) k_1^* \varepsilon_{11}(\boldsymbol{q}) - k_1 \left[\left(k_2^*\right)^2 \varepsilon_{22}(\boldsymbol{q}) + \left(k_3^*\right)^2 \varepsilon_{33}(\boldsymbol{q})\right] \\ +2\left(|\boldsymbol{k}|^2 - |k_1|^2\right) \left[k_2^* \varepsilon_{12}(\boldsymbol{q}) + k_3^* \varepsilon_{13}(\boldsymbol{q})\right] - 2k_1 k_2^* k_3^* \varepsilon_{23}(\boldsymbol{q}), \\ (d=3), \end{array} \right. \tag{2}$$

where the complex vector $\boldsymbol{k}$ defines the discretization method (see Willot, 2015):

$$k_j(\boldsymbol{q}) = \left\{ \begin{array}{cc} \mathrm{i} q_j, & \text{(FFT-MS)}, \\ \mathrm{e}^{\mathrm{i} q_j} - 1, & \text{(FFT-BF)}, \\ 2^{1-d} \mathrm{i} \tan\left(\frac{q_j}{2}\right) \left(1 + \mathrm{e}^{\mathrm{i} q_1}\right) \ldots \left(1 + \mathrm{e}^{\mathrm{i} q_d}\right), & \text{(FFT-R)}, \end{array} \right. \tag{3}$$

where $|\boldsymbol{k}|^2 = k_j k_j^*$, $\mathrm{i} = \sqrt{-1}$ and where k_j^* denotes the complex conjugate of k_j ($j = 1, \ldots, d$). The components of the Fourier wave vector $\boldsymbol{q}$ take on values $q_j = 2\pi n_j / M$ ($n_j = 1 - M/2, \ldots, M/2$) with M the number of voxels (or pixels) along each dimension. The forward and backward discrete Fourier transforms of a scalar field $g(\boldsymbol{x})$ is defined by:

$$g(\boldsymbol{q}) = \frac{1}{M^d} \sum_{\boldsymbol{x}} g(\boldsymbol{x}) \mathrm{e}^{-\mathrm{i} \boldsymbol{q} \cdot \boldsymbol{x}}, \qquad g(\boldsymbol{x}) = \sum_{\boldsymbol{q}} g(\boldsymbol{q}) \mathrm{e}^{\mathrm{i} \boldsymbol{q} \cdot \boldsymbol{x}}. \tag{4}$$

Circular permutations of the indicia in (2) give similar expressions for the other components u_2 and u_3. Note that mode $\boldsymbol{q} = 0$ is the rigid body motion, irrelevant in the solution.

3 Doubly-periodic array of cracks under plane strain

Consider now a 2D periodic array of cracks under plane strain. The elementary cell is discretized on two coarse and fine grids of $M \times M$ pixels with $M = 128$ and $M = 4096$. Both cells contain one single crack made of a row of

25 pixels ($M = 128$) or 800 pixels ($M = 4096$). In the following, we refer to a Cartesian coordinates system (e_x,e_y) with origin lying at a crack tip. By convention each crack is oriented along e_x and the size of the elementary cell is $L = 1$ (in arbitrary unit). The cracks length is therefore $\ell = 25/128 \approx 0.1953$.

Traction is applied so that $\overline{\sigma}_{xx} = \overline{\sigma}_{xy} = 0$ and $\overline{\sigma}_{yy} = 1$ GPa. In general, stress loadings are permitted by "dual" FFT schemes, that make use of the Green operator for the stress problem (Mura, 1982). However, these schemes cannot be used for porous media as they require one to use the compliance tensor (infinite in voids) rather than the stiffness tensor $\mathbf{C}$. Instead we achieve mode-I loading by applying a macroscopic strain field in three different directions, typically $\overline{\varepsilon}_{ij} = 1$ with $(i, j) = (1, 1)$, $(1, 2)$, $(2, 2)$, and compute mode-I fields by an appropriate linear combination of the resulting three solutions.

We compare numerical FFT-BF results for the elastic fields with the expansion for the singular stress fields near the crack-tip (Williams, 1957):

$$\sigma_{yy}(\boldsymbol{x}) = \cos\left(\frac{\theta}{2}\right)\left[1 + \sin\left(\frac{\theta}{2}\right)\sin\left(\frac{3\theta}{2}\right)\right]\frac{K_I}{\sqrt{2\pi r}} + \mathcal{O}(1) \tag{5}$$

where K_I is the stress intensity factor in mode I, $r \to 0$ is the distance from $\boldsymbol{x}$ to the crack tip and θ is the angle between direction $\mathbf{e}_x$ and the line joining $\boldsymbol{x}$ with the crack tip.

An estimate of K_I is obtained by the fit $\sigma_{yy} \sim 0.556/\sqrt{2\pi x}$ along a segment $y = 0$, $0 < x \ll L$ (Fig. 1, embedded graph), where the value 0.556 is expressed in GPa/$\sqrt{L}$ (GPa per square-root length unit). At fine resolution $M = 4096$, the square-root behavior near the crack-tip can be observed in a region of no more than one decade (solid black line) whereas it is not visible at coarse resolution ($M = 128$, purple dots). A fit over the $M = 4096$ data yields, for the normalized stress intensity factor $K_I' = K_I/\sqrt{\pi\ell/2}\overline{\sigma}_{yy} \approx 1.011$. This value is in agreement with the tabulated data obtained using a semi-analytical method by Karihaloo et al. (1996) and Karihaloo and Wang (1997) for doubly-periodic arrays of cracks. Indeed, the FFT prediction for $\ell/L = 0.195$ lies in-between two of the values provided by the authors, namely $K_I' \approx 1.003$ ($\ell/L = 0.1$) and $K_I' \approx 1.012$ ($\ell/L = 0.2$). Finite element computations carried out for the same problem, based on the method proposed by Delorenzi (1985), give $K_I' \approx 1.01128$.

The agreement between Eq. (5) and FFT results is confirmed by the field maps for the traction component σ_{yy} (Figs. 2a and 2c), computed at high resolution $M = 4096$. As observed in Fig. 1, the influence of neighboring cracks cannot be neglected far from the crack tip and FFT results differ significantly from Eq. (5). At coarse resolution $M = 128$, the field patterns are crudely represented (Fig. 2d). Nevertheless, this latter map resembles the locally-averaged maps (Fig. 2b), suggesting that local FFT values can be interpreted, roughly, as mean of the actual fields. Map (Fig. 2b) is computed by assigning to each voxel in the coarse grid the mean value of the asymptotic expansion (5), truncated to leading order.

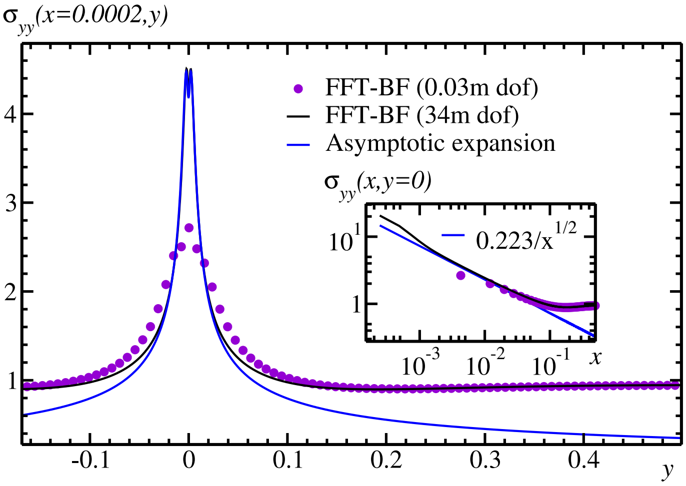

Figure 1: Periodic array of cracks in plane strain: profile of the stress component σ_{yy} along the segment $x = 2\,10^{-4}$, $-0.15 < y < 0.5$, close to the crack tip at $x = y = 0$. Solid black line and purple dots: Fourier backward-and-forward scheme with 34 millions and 32 thousands degrees of freedom. Solid blue line: asymptotic expansion near the crack tip (5) fitted with the value $K_I = 0.556$. Embedded graph (right): plot of σ_{yy} along the segment $y = 0$, $x > 0$, in log-log scale.

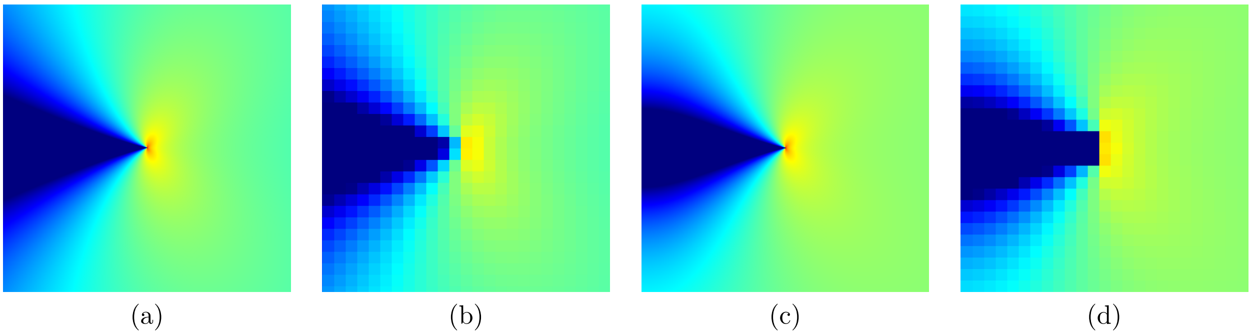

(a) (b) (c) (d)

Figure 2: Stress component σ_{yy} in a region centered around an isolated crack tip, in a 2D medium. (a): Asymptotic expansion (5); (c-d): FFT predictions for the backward-and-forward scheme (FFT-BF) on grids of 4096^2 (c) and 128^2 voxels (d); (b): local averages of the asymptotic expansion (a) on the same coarse voxel-grid as used in (d). The same color map, ranging from blue (lowest value) to red (highest value) is used in maps (a-d).

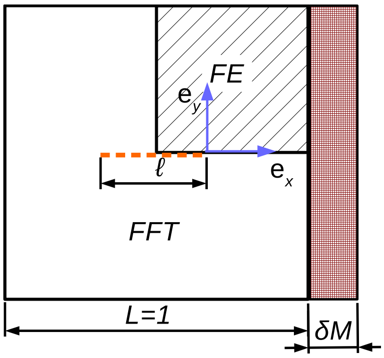

Figure 3: Computational domains used in finite element (dashed area, top-right) and FFT computations (white, dashed and crossed regions), showing the locations of the crack (dashed orange line) and axis (blue solid lines).

4 Local field around an isolated crack: finite element vs. Fourier methods

In this section, the accuracy of the local elastic fields predicted by Fourier and finite element methods are compared. We consider the Fourier schemes (FFT-BF) and (FFT-R) and two finite elements methods that use linear and quadratic elements, hereafter denoted (EF-L) and (EF-Q), respectively. The medium is made of a crack embedded in an isotropic matrix of Young modulus 1 and Poisson ratio 0.25. The crack, of length ℓ, is centered in a unit cell and oriented parallel to e_x. Here again, we refer to a Cartesian coordinates system with origin at the crack tip.

The FFT and FE methods employ boundary conditions that both result in mode-I crack opening under plane-strain. Using the finite element method, only one quarter of the cell is meshed taking advantage of the problem symmetry (see Fig. 3). Finite element simulations use a regular mesh of square elements. Linear (four Gauss points, four nodes) and quadratic (nine Gauss points, eight nodes) were used, respectively referred to as (FE-L) and (FE-Q). The stress field is evaluated at nodes using extrapolation of values at Gauss points. The crack tip lies at a node, located at coordinates $(0, 0)$. The vertical displacement is imposed to zero on the crack ligament ($0 < x \leq 1/2 - \ell/2$, $y = 0$) so as to allow crack opening while enforcing symmetry conditions. The horizontal displacement is also set to zero on the other symmetry line ($x = -\ell/2$, $0 \leq y \leq 1/2$). Normal displacements are imposed to be uniform (multi-point constraint condition) on the upper boundary ($y = 1/2$). A vertical force is imposed on the upper boundary so as to prescribe an average stress level $\overline{\sigma}_{yy} = 1$ within the cell. The last boundary ($x = 1/2 - \ell/2$) is stress-free. In contrast with Fourier methods, the crack is infinitely thin.

To obtain strictly equivalent boundary conditions using Fourier methods, we append to the "right" side of the cell, parallel to e_x, a porous layer of width $\delta M = 5$ voxels, obeying $\mathbf{C}(\boldsymbol{x}) \equiv 0$. This enforces the conditions $\sigma_{xx} = \sigma_{xy} = 0$ along $x = \pm 1/2 - \ell/2$ and, macroscopically, $\overline{\sigma}_{xx} = \overline{\sigma}_{xy} = 0$. More precisely, the elementary cell is now a rectangle $[-(1+\ell)/2; (1-\ell)/2+\delta M] \times [-1/2; 1/2]$ and the layer lies in the region $(1-\ell)/2 < x \leq (1-\ell)/2+\delta M$ (see Fig. 3). By periodicity, this layer is in contact with the opposite side $x = -(1 + \ell)/2$. As in Section 3, the crack is a row of pixels along the segment $-\ell \leq x < 0$, and plane strain loading is applied with $\overline{\varepsilon}_{yy} = 1$ and

$\bar{\varepsilon}_{xy} = \bar{\varepsilon}_{xx} = 0$. The mean stress field satisfies $\bar{\sigma}_{xx} = \bar{\sigma}_{yy} = 0$. Due to the symmetry of the problem with respect to $y = 1/2$, the periodic part of the displacement field $\boldsymbol{u}^* = \boldsymbol{u} - \bar{\boldsymbol{\varepsilon}} \cdot (\boldsymbol{x}, \boldsymbol{y})$ is zero along boundaries of the unit cell parallel to the crack ($u_x^* = u_y^* \equiv 0$ when $y = \pm 1/2$).

It is natural to assume that the crack tip lies between the last pixel in the crack and the pixel next to it in the matrix, in the same direction as the crack. Now, the strain and stress fields are estimated at the corners of each pixel in method (FFT-BF) and at pixel centers for (FFT-R). Hence, the crack tip is located at the center of a pixel edge for both methods. This edge is parallel to e_x for (FFT-BF) and parallel to e_y for (FFT-R). The origin of the Cartesian axis, chosen consistently with the discretization method, is shifted by one-half pixel in the two directions when comparing (FFT-R) with (FFT-BF). According to this definition of the Cartesian axis, the stress and strain fields are estimated at points with exactly the same coordinates. For instance, the point in the matrix closest to the crack tip is evaluated at a distance of one-half pixel in methods (FFT-BF) and (FFT-R). This is not so for the displacement field. In both methods, the displacement vector is estimated at the pixel's corners. Hence, the displacement is evaluated at Cartesian coordinates that are shifted by one-half pixel when comparing the two discretization methods. The two points closest to the crack tip where displacement is evaluated are at a distance of one-half pixel, in the direction parallel to the crack for method (FFT-BF) and transverse to it for method (FFT-R).

FFT computations are performed on grids containing $M^2 = 256^2$, 512^2, 1024^2, 2048^2 and 4096^2 voxels, whereas the number of elements in methods (FE-L) and (FE-Q) takes on values 64^2, 128^2, 256^2, 512^2. In the following, we compare Fourier and finite elements results as a function of the number of degrees of freedom (d.o.f.) for meshing or discretizing the entire unit cell. In practice, the number of d.o.f. is smaller by a factor of 4 for finite elements, as only one quarter of the unit cell has been meshed. The amount of memory needed for running the computations is much smaller when Fourier methods are used. For FE-Q computations with 1024^2 elements, for instance, 24 GB of memory were necessary when using the Z-Set software (Besson and Foerch, 1997) together with the Mumps Linear Solver (2017). Similar computations on grids of 1024^2 pixels used 58 MB of memory for methods (FFT-BF) of (FFT-R), using the Morphhom Software (2018).

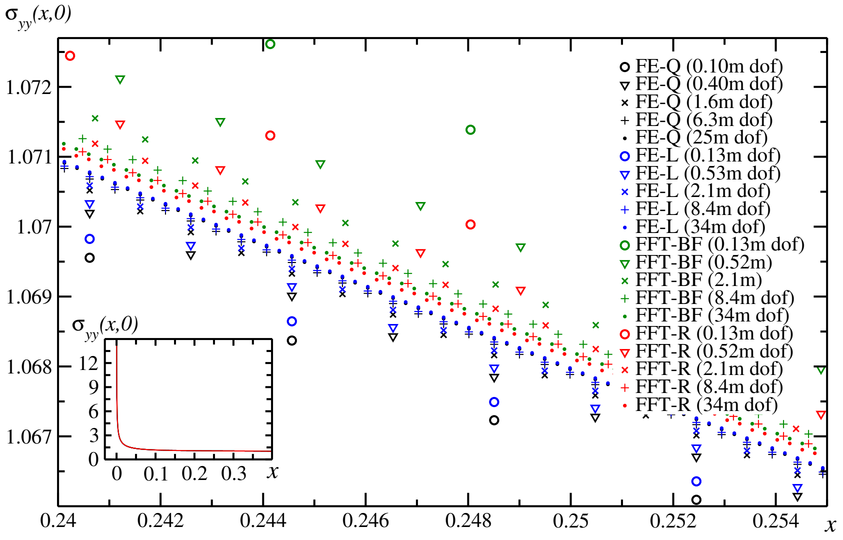

Figure 4: Profile of the stress component σ_{yy} along the segment $0.24 < x < 0.255$, $y = 0$: finite elements computations (linear elements in blue, quadratic in black) and FFT predictions (backward-forward scheme in green, rotated scheme in red). Each symbol denotes a comparable number of degrees of freedom (see legend, figures in millions). Bottom-left plot: σ_{xx} in the range $0 < x < 0.4$, predicted by methods (FE-Q), (FE-L), (FFT-BF) and (FFT-R) with about 30 millions number of degrees of freedom. The four curves cannot be distinguished from each other.

A profile of the stress component σ_{yy} along the segment that extends from the crack tip in direction $\mathbf{e}_x$ is shown in Fig. 4 in a region far from the crack tip and close to it (Fig. 5, in lin-log scale). In these plots and the following, the same symbols (e.g. circles, triangles, crosses) are used to denote similar number of degrees of freedom, whereas distinct colors distinguish the various methods (blue and black for FE, green and red for FFT). Overall, excellent agreement is found between all 4 methods for the entire profile (Fig. 4, embedded graph) with FE data points for the stress field converging by lower values and Fourier points by higher values (Fig. 4), except near the crack tip (Fig. 5). In general, the convergence rate for FE methods, as a function of the number of d.o.f., is somehow superior to Fourier methods, as in the region depicted in Fig. 4. In the same region, quadratic elements provide worse predictions than linear elements do at equivalent number of d.o.f. The predictions of the rotated scheme (FFT-R) are also clearly superior to that of the backward-and-forward scheme (FFT-BF). Near the crack tip, the predictions by finite element methods of the stress component σ_{yy} is nearly as accurate as that offered by Fourier methods (Fig. 5). At low number of d.o.f., method (FFT-BF) gives the most accurate predictions (Fig. 5, see also embedded graph in log-log scale). Although method (FFT-R) uses, contrarily to (FFT-BF), more precise centered differences, the finite-difference scheme used in (FFT-BF) is more "local" than in (FFT-R). Derivatives are estimated by differences taken over points that lie at a distance of $1/L$ from each other in method (FFT-BF), and $\sqrt{2}/L$ in method (FFT-R).

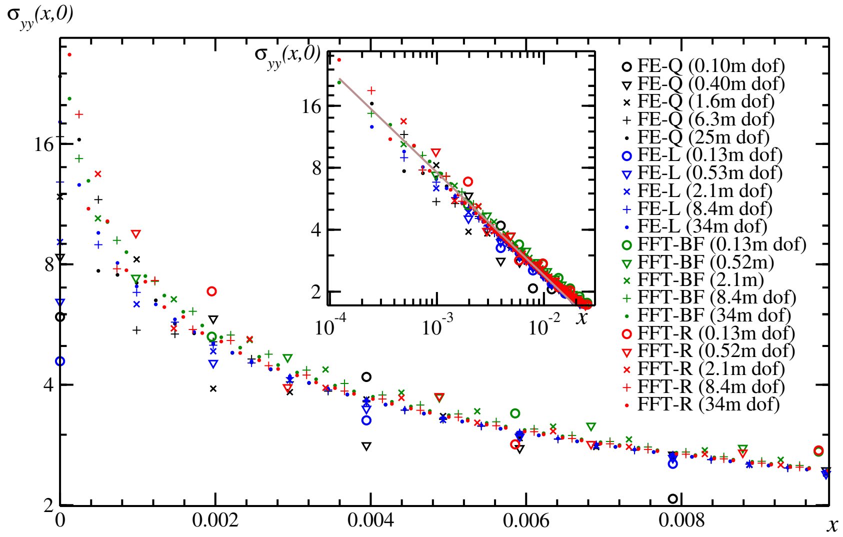

Figure 5: Profile of the stress component σ_{yy} along the line $y = 0$ extending from an isolated crack in a 2D medium, in lin-log scale: finite element computations (linear elements in blue, quadratic in black) and FFT predictions (backward-forward scheme in green, rotated scheme in red). Each symbol denotes a comparable number of degrees of freedom (see legend, figures in millions). Top-right, embedded graph: same data in log-log scale. Solid brown line: function $0.564/\sqrt{2\pi x}$ with x the distance to the crack tip.

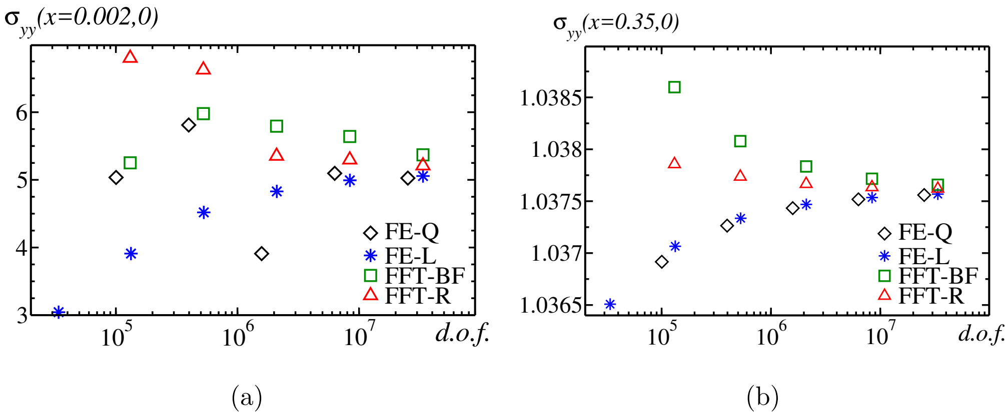

(a)

(b)

Figure 6: Continuation of Figs. 5 and 4: prediction of the stress component σ_{yy} at two points as a function of the number of degrees of freedoms: finite elements with linear elements (stars), quadratic elements (diamonds), backward-forward (squares) and rotated (triangles) Fourier schemes. (a) Point ($x = 0.002$, $y = 0$) near the crack-tip. (b) Point ($x = 0.35$, $y = 0$) far from the crack.

As for finite elements, quadratic elements (Fig. 5, black symbols) are less accurate than linear elements (blue symbols). For instance, close to the crack tip, the predictions obtained with 1.6 millions of d.o.f. and quadratic elements (black crosses) are less accurate than obtained with 530 thousands d.o.f. and linear elements (blue triangles). As in the case of the FFT computations, simple discretization methods produce better estimates, in the vicinity of the crack tip, where the stress field is singular and unbounded.

Numerical FE and FFT predictions for the stress component σ_{yy} are plotted in Fig. 6 as a function of the number of d.o.f. Two points along the line $y = 0$ are considered. Close to the crack tip, convergence is erratic (Fig. 6a), except for the predictions of method (EF-L) which are remarkably regular with respect to the number of d.o.f. Also, the good-behavior of scheme (FFT-BF) at coarse resolutions does not extend to finer resolutions. Although FE methods give more accurate predictions than Fourier methods in the region observed in Fig. 4, this is not so at a point closer to the boundary (Fig. 6b). At this point, methods (FE-L) and (FE-Q) give equivalent predictions, but not better than (FFT-R).

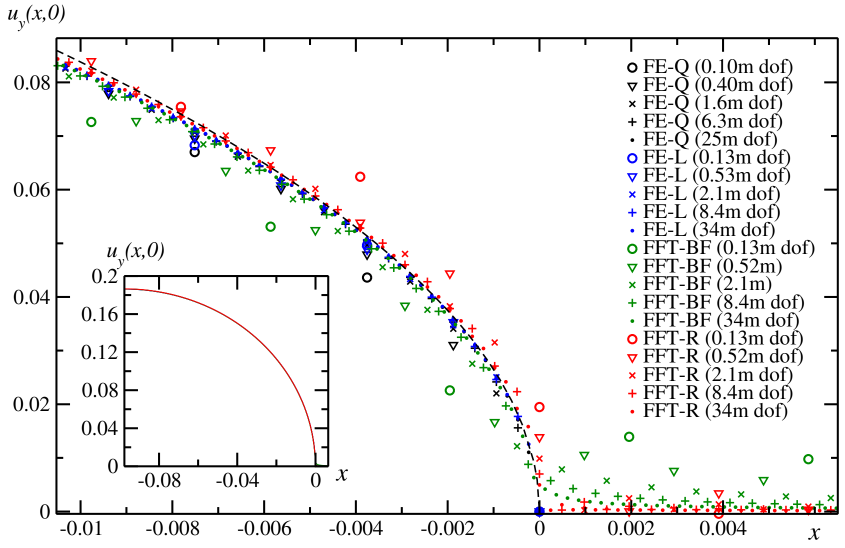

Figure 7: Profile of the displacement component u_y along the line $y = 0$ extending from an isolated crack in a 2D medium, in a small segment containing the crack tip: finite element computations (linear elements in blue, quadratic in black) and FFT predictions (backward-forward scheme in green, rotated scheme in red). Each symbol denotes a comparable number of degrees of freedom (see legend, figures in millions). Bottom-left: displacement u_y along one-half of the crack $-0.098 < x < 0$, predicted by finite element and FFT computations $FE - Q$, $FE - L$, $FFT - BF$ and $FFT - R$ with about 30 millions number of degrees of freedom. The displacement is set to 0 at point $y = 0$, $x = 1/2 - 0.098$.

The accuracy of the various methods for estimating the displacement field is examined in Figs. 7, 8, and 9. Again, the agreement between the various methods for the displacement component u_y, which is discontinuous along the crack, is excellent (Fig. 7, embedded graph). A segment of line that contains a portion of the crack, including the crack tip, and part of the embedding medium is represented in Fig. 7. The asymptotic behavior of u_y near the crack tip is represented in black (dashed line). It is given by Williams (1957):

$$u_y = \frac{K_I}{2\mu}\sqrt{\frac{r}{2\pi}}\sin\frac{\theta}{2}\left(4 - 4\nu - 2\cos^2\frac{\theta}{2}\right), \qquad r \to 0, \tag{6}$$

where $\mu = 0.4$ is the shear modulus.

The predictions of (FFT-R) are more accurate than (FFT-BF) outside the cracks, and to a lesser extent inside the crack. Overall, Fourier estimates are less accurate than their FE counterpart near the crack tip. In FE methods, u_y is strictly zero whenever $y = 0$ and $x > 0$, as enforced by the boundary conditions. This is not so in FFT methods, where u_y is set to zero at a single point far from the crack tip ($y = 0$, $x = (1 - \ell)/2$). The behavior is confirmed in Fig. 9b where the predictions of all four methods are plotted as a function of the number of d.o.f. The same trend is observed in the middle of the crack (Fig. 8) except for scheme (FFT-BF) which gives surprisingly good estimates (see also Fig. 9a).

Overall, FE and Fourier methods provide reliable estimates for both the displacement and stress fields, except in a narrow region near the crack tip. FE methods yield somewhat more accurate predictions, in particular with

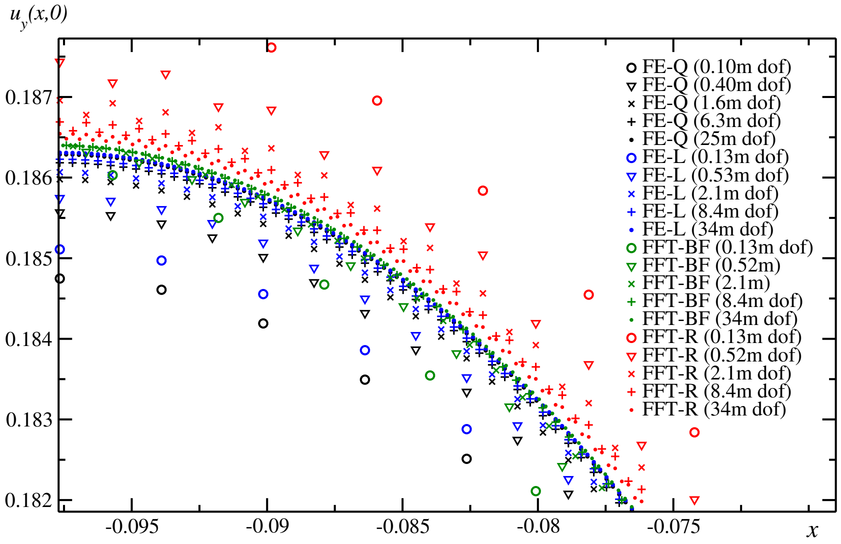

Figure 8: Continuation of Fig. 7: profile of the displacement component u_y in a segment of line close to the middle of the crack ($y = 0$, $-0.098 < x < -0.073$).

linear elements. This is not surprising as these methods model perfectly-thin cracks, contrarily to Fourier methods. Boundary conditions also play a role in this comparison. In the computations we carried out, FE methods predict no displacement in mode-I along the line that extends the crack, which is the exact result, in contrast with FFT methods. Conversely, Fourier methods predict a strictly-zero stress field along the crack, contrarily to FE computations (not shown in the figures). Fourier results are satisfactory, yet the problem examined here involves a favorable configuration where the crack is aligned with the voxel grid or with the mesh elements. In the next section, we explore the role of grid-discretization in situations where the cracks are not oriented parallel to the voxel edges.

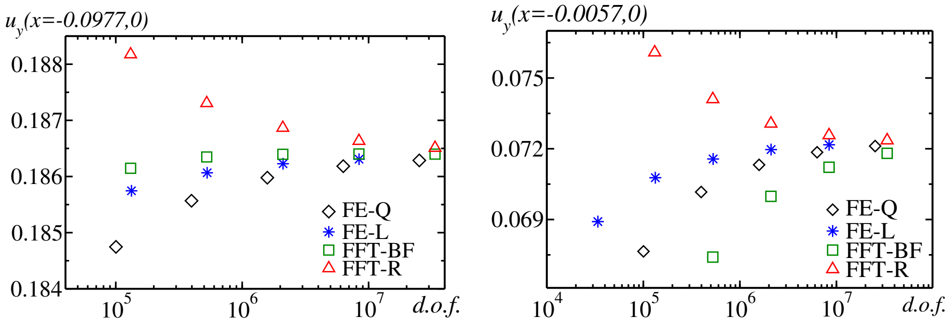

(a) (b)

Figure 9: Continuation of Figs. 7 and 8: one value of the displacement component u_y in the middle of the crack ($y = 0$, $x = -0.977$) (a) and near the crack-tip ($y = 0$, $x = -0.0057$) (b), as a function of the number of degrees of freedom: finite element with linear elements (stars), quadratic elements (diamonds), Fourier methods with backward-forward (squares) and rotated (triangles) schemes.

5 Effective response of a body containing disk-shaped cracks

5.1 Periodic array of parallel cracks

This section is concerned with the effect of grid discretization, the orientation and the crack thickness on the effective elastic moduli , in dimension 3. Consider first a single crack embedded in the unit elementary cell Ω.

The crack has a cylindrical shape with varying width w and radius 0.2. The embedding matrix is elastic-isotropic with Young modulus $E^{\text{mat}} = 1$, shear modulus $G^{\text{mat}} = 0.4$ and Poisson ratio $\nu^{\text{mat}} = 0.25$. The Cartesian axis are aligned with the voxel edges. We consider cracks oriented parallel to the grid, e.g. parallel to e_x and e_y and normal to e_z (denoted "parallel cracks"). To address the effect of grid orientation with respect to the crack's normal, we also consider "transverse cracks" oriented along a plane at equal angle from e_x, e_y and e_z, i.e. perpendicular to $\mathrm{e}_x + \mathrm{e}_y + \mathrm{e}_z$. To explore the influence of the crack thickness w, we compute FFT data points for parallel cracks with thickness $w = 1$ up to $w = 13$ voxels. For transverse cracks, the thickness take on increasing values $w = 1/\sqrt{3} \approx 0.58$, $\sqrt{3} \approx 1.73$ up to 12.1. These values correspond to an increase of the number of voxels in the cracks after discretization. When $w = 1/\sqrt{3}$, the crack's voxels are connected through their edges and corners only, not by their faces.

The effective response of the material is described by the transversely-isotropic compliance tensor:

$$\mathbf{S} = \begin{pmatrix} 1/E_p & -\nu_p/E_p & -\nu_{pz}/E_p & 0 & 0 & 0 \\ & 1/E_p & -\nu_{pz}/E_p & 0 & 0 & 0 \\ & & 1/E_z & 0 & 0 & 0 \\ & & & 1/G_{zp} & 0 & 0 \\ & \text{sym} & & & 1/G_{zp} & 0 \\ & & & & & 2\left(1+\nu_p\right)/E_p \end{pmatrix}, \tag{7}$$

with five independent elastic moduli $E_{p,z}$, G_{zp}, $\nu_{p,pz}$ and $\nu_{zp} = (E_p/E_z)\nu_{pz}$. The form above refers to the following Voigt notation:

$$(\bar{\varepsilon}_{11}, \bar{\varepsilon}_{22}, \bar{\varepsilon}_{33}, 2\bar{\varepsilon}_{23}, 2\bar{\varepsilon}_{13}, 2\bar{\varepsilon}_{12})^{\text{t}} = \mathbf{S} \cdot (\bar{\sigma}_{11}, \bar{\sigma}_{22}, \bar{\sigma}_{33}, \bar{\sigma}_{23}, \bar{\sigma}_{13}, \bar{\sigma}_{12})^{\text{t}}. \tag{8}$$

The moduli in (7) are computed numerically using schemes (FFT-R), (FFT-BF) and (FFT-MS) on grids of 128^3 voxels. Macroscopic strain loadings are applied in appropriate directions to recover all moduli. The FFT predictions for the effective response are compared to the Eshelby-type solution for the strain and stress fields occurring in an isolated ellipsoidal pore in a homogeneous medium, derived by Sevostianov et al. Sevostianov et al. (2005). In this solution, the pore shape is an ellipsoid of revolution. The limiting case of an infinitely-thin oblate ellipsoid, i.e. a disk, gives the effective moduli of a set of non-interacting open cracks parallel to each other. This solution shows that the Poisson ratios $\nu_p = \nu_{pz} = \nu^{\text{mat}}$, and, obviously, the Young modulus $E_p = E_p^{\text{mat}}$ are not affected by the presence of cracks while the elastic moduli G_{zp}, E_z and Poisson ratio ν_{zp} are influenced by the crack.

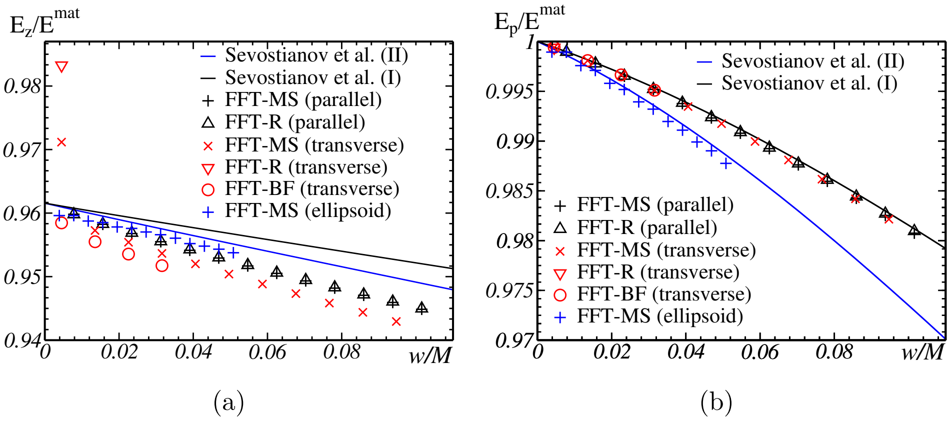

Figure 10: Influence of the crack's width w on the effective elastic moduli of a periodic array of cracks: Young moduli E_z and E_p. Symbols: FFT data points for cracks with cylindrical shape oriented parallel (black) and transverse (red) to the voxel grid and for ellipsoidal cracks with axis parallel to the voxel grid (blue). Solid lines: exact result for non-interacting parallel ellipsoidal voids. Black: with the same volume as the cylinders (method I). Blue: with lowest semi-axis $w/2$ (method II).

FFT results and analytical estimates are shown in Figs. 10, 11 and 12 for the 6 normalized effective moduli as a function of the ratio w/M. In all plots, FFT data points are represented by symbols colored in black for parallel cracks and red for transverse ones. Methods FFT-R (triangles), FFT-MS (+, ×) and FFT-BF (circles) are used. For the latter method, only the transverse type is considered. The analytical result in Sevostianov et al. (2005) is represented by two solid lines in each plot. In method I (black), the ellipsoidal inclusion has the same volume fraction as the cylinder for a given w, and $w/2$ is not the ellipsoid's lowest semi-axis. In method (II), $w/2$ is the lowest semi-axis of the ellipsoidal inclusion and the ellipsoid and cylinder volumes are different. As expected, the FFT data points for E_z/E^{mat}, G_{zp}/G^{mat} and $\nu_{zp}/\nu^{\mathrm{mat}}$ converge to a value lower than 1 and to 1 for the other normalized moduli, as predicted by the theory. A small discrepancy is observed for the limiting value of E_z/E^{mat} and G_{zp}/G^{mat} predicted by the analytical result and by FFT computations. This is because the non-interacting assumption is not valid for the periodic boundary conditions used in the FFT computations.

A larger discrepancy is observed between the analytical result (solid lines) and FFT points (red and black symbols) for finite values of w. To interpret this difference, we carried out additional FFT computations with ellipsoidal voids using the method FFT-MS (+ symbols, in blue). Its semi axis are parallel to the voxel grid. The highly-oblate ellipsoidal voids are quite crudely discretized on the 128^3-voxels grid as shown by the erratic variations predicted for ν_{pz}. Nevertheless, they yield estimates that are much closer to the analytical results (solid blue line). This is especially obvious for the Poisson coefficients ν_p (Fig. 11b) ν_{zp} (Fig. 12a) and ν_{pz} (Fig. 12b). The data for ν_{zp} show that this coefficient is nearly constant for cylinders, and increases with w for ellipsoidal voids. Clearly, the FFT data for ellipsoids are different from the exact result, as shown in Fig. 11a for the shear modulus G_{zp}, but again, the discretization of highly-oblate ellipsoids on the grid is poor.

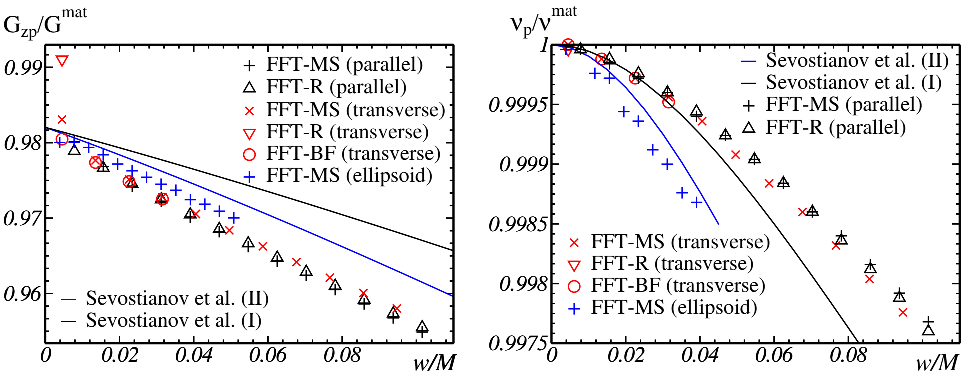

(a) (b)

Figure 11: Continuation of Fig. 10: shear modulus G_{zp} and Poisson ratio ν_p.

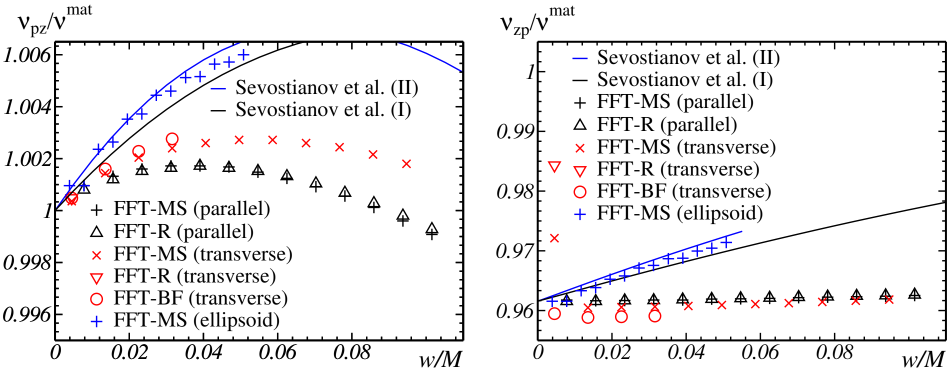

(a) (b)

Figure 12: Continuation of Fig. 11: Poisson ratios ν_{pz} and ν_{zp}.

FFT data points related to transverse cracks (red symbols) agree very well with that of parallel cracks except for two important cases. First, for values of w larger than 1, FFT predictions slightly underestimate E_z when compared to the values obtained for parallel cracks. The same remark applies to ν_{zp}, which is directly related to E_z. Second, the predictions obtained for transverse cracks with the lowest value of w are significantly overestimated for schemes (FFT-R) and (FFT-MS), but not (FFT-BF). This applies to all moduli influenced by the crack in the limit $w \to 0$, i.e. G_{zp}, E_z and ν_{zp}. We interpret this result as a consequence of the Fourier methods's underlying discretization schemes. In method (FFT-R), stress can be transmitted along the voxel diagonals and across voxel corners, where the divergence of $\boldsymbol{\sigma}$ is evaluated. This applies to transverse cracks when w takes its lowest value. In this configuration, it is possible to draw a line that crosses the crack while staying in the matrix everywhere except at a single point (a voxel corner). This significantly increases the Young modulus transverse to the crack. A similar phenomenon is observed for method (FFT-MS). This problem does not apply to method (FFT-BF) where stress transmission occurs between voxels that share a common face only. As a consequence, (FFT-BF) predictions are accurate for transverse crack even when w takes its lowest value. This property is especially useful for taking into account a large number of cracks, discretized using a thickness as small as possible.

5.2 Parallel, randomly-distributed cracks

In order to evaluate method (FFT-BF) for predicting the effective moduli of a randomly-cracked medium, we carry out additional computations in dimension 3. As before, the cracks are cylinders of radius $a = 0.2$ and width $w = 1$ voxel and are embedded in a matrix with Young modulus 1 and Poisson ratio 0.25. The cracks are parallel to each other and the axis of symmetry of the cylinders are aligned with e_3. However, they are now located at random positions. The crack centers are chosen uniformly in the unit cell with one restriction: the cracks are forbidden to overlap or touch one another. A domain Ω of volume V containing $n = 1$, 10, 21, 30, 62 and 92 cracks is considered. The density of cracks is monitored by the dimensionless parameter (introduced by Bristow, 1960):

$$\eta = \frac{na^3}{V}. \tag{9}$$

FFT results for the effective elastic moduli are represented in Fig. 13 as circles, and are compared to the “non-interacting” approximation of Kachanov, 1992 (solid blue line) and to the self-consistent scheme of Hoenig, 1979 (solid green line). Two effective moduli are considered: the shear modulus G_{zp} (Fig. 13b). as well as the bulk modulus (Fig. 13a) defined by:

$$K = \left[\frac{2(1 - \nu_p - 2\nu_{pz})}{E_p} + \frac{1}{E_z} \right]^{-1}. \tag{10}$$

The numerical and analytical estimates are very close to one another in the dilute crack-density regime ($\eta \lessapprox 0.1$). In the domain $0.1 \leq \eta \leq 0.2$, FFT data points are close to the estimate of Sevostianov et al. for the bulk modulus and to Hoenig's formula for the shear modulus. Recall however that, as an effect of the finite thickness of the cracks, FFT predictions underestimate the effective elastic moduli. As expected, the numerical results differ from the analytical estimates for large crack density ($\eta \geq 0.2$).

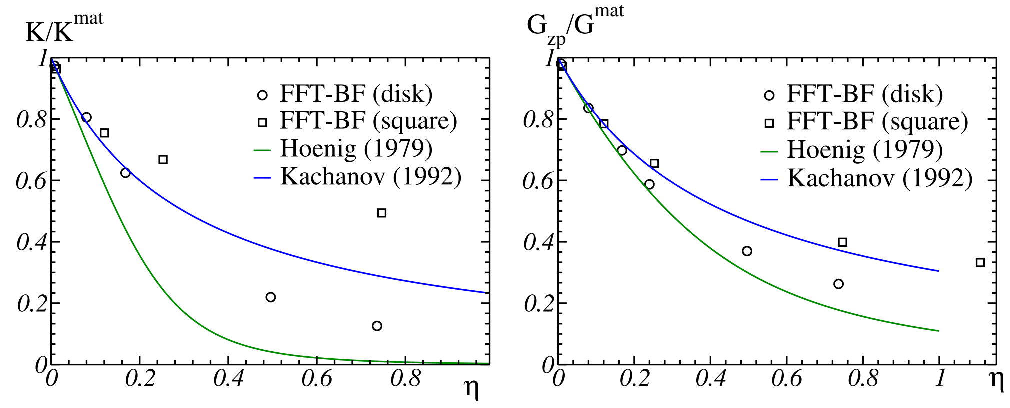

(a)

(b)

Figure 13: Normalized effective bulk modulus $\widetilde{K}/K^{\mathrm{mat}}$ (a) and shear modulus $G_{zp}/G_{zp}^{\mathrm{mat}}$ (b), of a random array of parallel cracks for increasing crack density η. The cracks have a cylindrical shape of width $w = 1$ voxel and either circular (black disks) or square cross section (black squares). Solid lines: homogenization theories for a matrix containing a random set of parallel elliptical cracks. Blue: “non-interacting” approximation (Kachanov, 1992); Green: estimate of Hoenig (1979).

In order to address the effect of the cracks shape, we run additional computations using cylinders with a square basis for the cracks. The squares have side length ℓ and are parallel to the plane (e_1; e_2). The crack-density parameter is computed using the same formula as for the disks (9), where a is the radius of the disk with same surface area as the squares ($a = \ell/\sqrt{\pi}$). Results for the effective elastic moduli are shown in Fig. 13, as square symbols. The bulk K and shear moduli G_{zp} obtained for squares and disks are similar when $\eta \leq 0.2$ and significantly different when $\eta \geq 0.2$. Obviously, the definition of η for non-elliptic shapes has an important role in this comparison.

5.3 Randomly-oriented cracks

The accuracy of the method is now studied in the context of randomly-oriented, possibly-intersecting cracks, in 3D. Specifically, we consider a homogeneous body with isotropic elastic response and Poisson ratio $\nu = 0.2$, containing a set of disk-shaped cracks. The cracks have random, uniformly-distributed orientation and their centers are uniformly distributed in Ω. We restrict our analysis to a fixed density of cracks $\eta = 0.3815$. The domain Ω is discretized on grids of $M^3 = 128^3$, 256^3, 512^3, 1024^3 and 1944^3 voxels, the cylindrical cracks have a diameter of $2a = 40$, 80, 160 or 223.8 voxels and the thickness take on increasing values $w = 1.25$, 1.4, 1.5, 2, 3, 4 and 5 voxels. The number of cracks n, adjusted so that the crack-density remains equal, i.e. $n = \eta(M/a)^3$, varies between $n = 100$ cracks and $n = 2000$ cracks. Three configurations (A), (B) and (C) are considered, corresponding to two independent realizations of the Boolean random set in the continuum. For a given configuration, the number, positions and orientations of the cracks are fixed, although discretization on a grid depends on M, w and a. The Poisson ratio in the matrix is 0.2 and the Young modulus is 1.

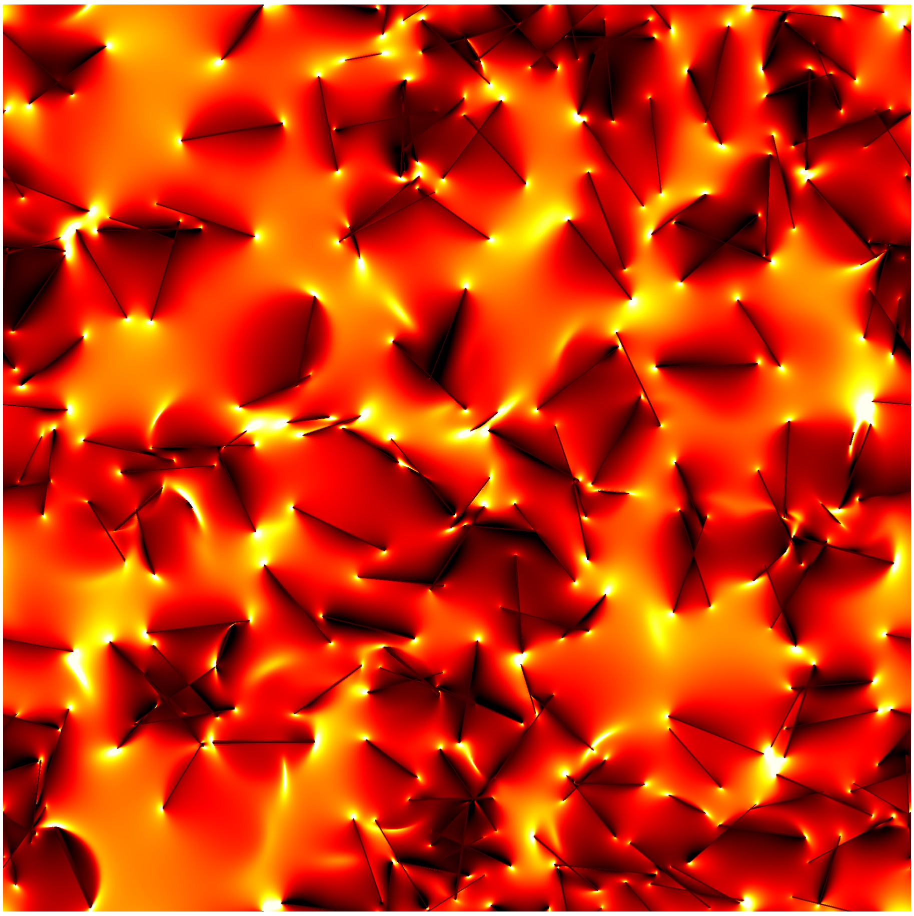

Figure 14: FFT map of the stress component σ_m with applied macroscopic strain $\langle \varepsilon_{ij} \rangle = \delta_{ij}$ and crack density $\eta = 0.3815$ (2D cut), in a volume containing 2,000 cracks of diameter 224 voxels, discretized on a grid of 1944^3 voxels. The stress field is thresholded in the range $[-0.22; 2.6]$ to highlight the fields patterns (highest values in white, lowest in black). In this range, 0.5% of the lowest and highest stress values have been thresholded out.

The backward-and-forward difference scheme (FFT-BF) is used. A map of the stress component σ_m when hydrostatic strain loading is applied is represented in Fig. 14 at the finest resolution $M = 1944$. FFT results for the apparent bulk modulus K (normalized by the bulk modulus K^{mat} in the solid) are represented in Fig. 15 as a function of the cracks's aspect ratio $w/(2a)$. In order to minimize the effect of the cracks thickness, the apparent modulus is estimated by:

$$K = \frac{\langle \sigma_m \rangle}{3(1-f)\overline{\varepsilon}_m}, \qquad 3\overline{\varepsilon}_m = \mathrm{tr}(\overline{\boldsymbol{\varepsilon}}), \qquad 3\sigma_m = \mathrm{tr}(\boldsymbol{\sigma}), \tag{11}$$

where hydrostatic loading is applied ($\overline{\varepsilon}_{ij} = \delta_{ij}$) and f is the porosity. Thus, $\langle \sigma_m \rangle/(1-f)$ is an estimate of the

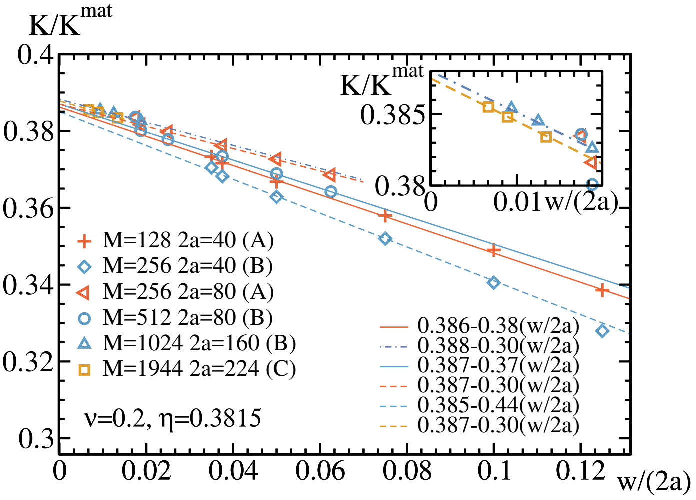

Figure 15: FFT estimates for the normalized bulk modulus $\widetilde{K}/K$ in a homogeneous isotropic body ($\nu = 0.2$) containing a population of cracks with density $\eta = 0.3815$: effect of the cracks aspect ratio $w/(2a)$ for three configuration A (red), B (blue) and C (orange) of the Boolean model of cracks, with various grid-resolutions $M = 128$, 256, 512, 1024, 1944 voxels.

mean of the resulting stress field, as if the cracks had no volume.

For a given grid resolution (i.e. at fixed value of M) and given configuration, we observe a linear trend $K \approx K_0 + c(w/2a)$ with $c \leq 0$, in the domain $w \geq 1.5$ (Fig. 15, solid and dotted lines). Numerical predictions overestimate the effective moduli at points $w = 1.25$ and $w = 1.4$. The limit of K when $w \to 0$ is extrapolated from the data obtained with $w \geq 1.5$. The effect of the cracks aspect ratio can be estimated by comparing a coarse ($M = 256$, $2a = 40$), intermediate ($M = 512$, $2a = 80$) and fine discretization ($M = 1024$, $2a = 160$) of the same configuration B (blue symbols). The three cases, each containing 800 cracks, yield very close limiting values 0.385 0.387 and 0.388 for the bulk modulus K when $w \to 0$. The best estimates for configurations B (with $M = 1024$) and C (with $M = 1944$) yield nearly the same estimate ($K \approx 0.388$ and $K \approx 0.387$, resp.). These values are close to the self-consistent estimate $K \approx 0.4036$ provided by Willot et al. (2018).

6 Conclusion

This first part of the work has shown that cracks, discretized on a voxel grid as thin porous inclusions, can be accounted for using Fourier-based numerical schemes. Microcrack populations embedded in a homogeneous matrix have been accounted for as well within in a full-field homogenization Fourier-based methodology, with an accuracy comparable to that of finite element techniques. A relative error on the effective bulk modulus of less than 1% has been obtained using the proposed method on a grid of 512^3 voxels containing 800 randomly-oriented cracks in 3D. The drawback of the method, namely its inability to represent zero-volume cracks, can be coped with, in particular with the backward-and-forward finite-difference Fourier scheme, provided the thickness of the cracks is larger than 1.5 voxels. Although this discretization technique does not treat all grid directions symmetrically (Willot and Pellegrini, 2008), it offers, in this context, the most accurate fields when dealing with arbitrarily-oriented cracks.

Acknowledgments

The authors gratefully acknowledge the financial support of the French Commissariat à l'Énergie Atomique.

References

Andrieux S., Bamberger Y., Marigo J.-J., Un modèle de matériau microfissuré pour les bétons et les roches, *J. Méca. Théor. Appl.* **5** (3), 1986, 471–513.

Bargellini R., Halm D. and Dragon A., Modelling of quasi-brittle behaviour: a discrete approach coupling anisotropic damage growth and frictional sliding, *Eur. J. Mech. A/Solids* **27**, 2008, 564–581.

Besson J. and Foerch R., Large scale object–oriented finite element code design, *Comp. Meth. Appl. Mech. Eng.* **142**, 1997, 165–187.

Bristow J. R., Microcracks, and the static and dynamic elastic constants of annealed and heavily cold-worked metals, *Br. J. Appl. Phys.* **11** (2), 1960, 81.

Budiansky B., O'Connell R. J., Elastic moduli of a cracked solid, *Int. J. Solids Struct.* **12** (2), 1976, 81–97.

Challamel N., A variationally based nonlocal damage model to predict diffuse microcracking evolution., *Int. J. Mech. Sci.* **52**, 2010, 1783–1800.

Cheng Y., Damage mechanisms of sic/sic composite tubes: three-dimensional analysis coupling tomography imaging and numerical simulation, 2017, University Paris-Est, Ph.D. thesis.

Cormery F. and Welemane H., A critical review of some damage models with unilateral effect., *Mech. Res. Comm.* **29**, 2002, 391–395.

Cormery F. and Welemane H., A stress-based macroscopic approach for microcracks unilateral effect., *Comput. Mat. Sci.* **47**, 2010, 727–738.

Delorenzi H. G., Energy release rate calculations by the finite element method, *Eng. Fract. Mech.* **21** (1), 1985, 129–143.

Dormieux L. and Kondo D., Stress-based estimates and bounds of effective elastic properties: the case of cracked media with unilateral effects., *Comput. Mat. Sci.* **46** (1), 2009, 173–179.

Eyre D. J. and Milton G. W., A fast numerical scheme for computing the response of composites using grid refinement, *Eur. Phys. J. Appl. Phys.* **6** (1), 1999, 41–47.

Hoenig A., Elastic moduli of a non-randomly cracked body, Int. J. Solids Struct. 15 (2) (1979) 137–154.

Horii H. and Nemat-Nasser S., Overall moduli of solids with microcracks: load-induced anisotropy, *J. Mech. Phys. Solids* **31**, 1983, 155–171.

Huang Y. and Hu K. X., Elastic moduli of a microcracked composite with spherical inclusions of cubic anisotropy, *Compos. Sci. Technol.* **50** (2), 1994, 149–156.

Kachanov M., Effective elastic properties of cracked solids: critical review of some basic concepts, *Appl. Mech. Rev.* **45** (8), 1992, 304–335.

Karihaloo B. L., Wang J. and Grzybowski M., Doubly periodic arrays of bridged cracks and short fibre-reinforced cementitious composites, *J. Mech. Phys. Solids* **44** (10), 1996, 1565–1586.

Karihaloo B. L. and Wang J., On the solution of doubly periodic array of cracks, *Mech. Mater.* **26** (4), 1997, 209–212.

Krajcinovic D., Damage mechanics, *Mech. Mat.* **8**, 1989, 117–197.

Levasseur S., Welemane H. and Kondo D., A microcracks-induced damage model for initially anisotropic rocks accounting for microcracks closure., *Int. J. Rock Mech. & Min. Sci.* **77**, 2015, 122–132.

Li J., Meng S., Tian X., Song F. and Jiang C., A non-local fracture model for composite laminates and numerical simulations by using the FFT method, *Compos. Part B* **43** (3), 2012, 961–971.

Li J., Tian X.-X. and Abdelmoula R., A damage model for crack prediction in brittle and quasi-brittle materials solved by the FFT method, *Int. J. Fract.* **173** (2), 2012, 135–146.

Michel J.-C., Moulinec H. and Suquet P., A computational scheme for linear and non-linear composites with arbitrary phase contrast, *Int. J. Numer. Meth. Eng.* **52** (1–2), 2001, 139–160.

Monchiet V., Gruescu C., Cazacu O. and Kondo D., A micromechanical approach of crack-induced damage in orthotropic media: application to a brittle matrix composite, *Eng. Fract. Mech.* **83**, 2012, 40–53.

Morphhom Software, `http://cmm.ensmp.fr/morphhom`, accessed february 23, 2018.

Moulinec H. and Suquet P., A fast numerical method for computing the linear and non linear mechanical properties of the composites, *Comptes Rendus Acad. Sci. Série II* **318**, 1994, 1417–1423.

Mumps Linear Solver, 2017, `http://graal.ens-lyon.fr/MUMPS`.

Mura T., Micromechanics of defects in solids, Martinus Nijhoff Publishers, 1982, Martinus Nijhoff Publishers, The Hague.

Ortiz M., A constitutive theory for the inelastic behavior of concrete, *Mech. Mater.* **4** (1), 1985, 67–93.

Pensée V. and Kondo D., Micromechanics of anisotropic brittle damage: comparative analysis between a stress based and a strain based formulation, *Mech. Mat.* **35**, 2003, 747–741.

Pijaudier-Cabot G. and Bazant Z.-P., Nonlocal damage theory, *J. Eng. Mech.* **113**, 1987, 1512–1533.

Sevostianov I., Yilmaz N., Kushch V. and Levin V., Effective elastic properties of matrix composites with transversely-isotropic phases, *Int. J. Solids Struct.* **42** (2), 2005, 455–476.

Williams M. L., On the stress distribution at the base of a stationary crack, *J. Appl. Mech.* **24**, 1957, 109–114.

Willot F. and Pellegrini Y.-P., Fast Fourier transform computations and build-up of plastic deformation in 2D, elastic-perfectly plastic, pixelwise-disordered porous media, In: Jeulin D., Forest S. (Eds.), *Continuum Models and Discrete Systems CMDS 11, École des Mines, Paris,* 2008, 443–449. Online at `http://arxiv.org/abs/0802.2488`.

Willot F., Fourier-based schemes for computing the mechanical response of composites with accurate local fields, *Comptes Rendus Mec.* **343** (3), 2015, 232–245.

Willot F., Trumel H. and Jeulin D., The thermoelastic response of cracked polycrystals with hexagonal symmetry, *Phil. Mag.* **99** (5), 2019, 606–630.

Yan P., Delannay L., Payne J. and Tzelepi A., Micromechanistic modelling of the polycrystalline response of graphite under temperature changes and irradiation, *Carbon* **96**, 2016, 827–835.

Zhu Q.-Z., Shao J. F. and Kondo D., A micromechanics-based thermodynamic formulation of isotropic damage with unilateral and friction effects., *Eur. J. Mech. A/Solids* **30**, 2011, 316–325.